Metamaterial-Based Low-Profile Broadband Aperture-Coupled Grid-Slotted Patch Antenna

Wei Liu, Zhi Ning Chen, and Xianming Qing

***Abstract*—A metamaterial-based broadband low-profile grid-slotted patch antenna is presented. By slotting the radiating patch, a periodic array of series capacitor loaded metamaterial patch cells is formed, and excited through the coupling aperture in a ground plane right underneath and parallel to the slot at the center of the patch. By exciting two adjacent resonant modes simultaneously, broadband impedance matching and consistent radiation are achieved. The dispersion relation of the capacitor-loaded patch cell is applied in the mode analysis. The proposed grid-slotted patch antenna with a low profile of $0.06\,\lambda_0$ (λ_0 is the center operating wavelength in free space) achieves a measured bandwidth of 28% for the $|S_{11}|$ less than -10 dB and maximum gain of 9.8 dBi.**

***Index Terms*—Aperture coupling, broadband antenna, capacitor-loaded patch cell, low profile, metamaterial, patch antenna, transmission-line model, wide bandwidth.**

I. Introduction

With the advancement of modern wireless communication systems, broadband antennas are of increasing demand. Microstrip patch antennas have been received much attention because of their low profile, light weight, low cost, compatible with printed circuits, although they suffer from narrow impedance bandwidth. Many techniques have been reported to overcome the drawback of the inherent narrow bandwidth, including the utilization of capacitive probe feed, L-probe feed, aperture coupling, U/E-slotted patch, and stacked patches [1]–[6]. However, a thick substrate with low dielectric constant is usually required and therefore, it is difficult to make the antenna low-profile. We have proposed a unique broadband low-profile antenna design methodology using a composite right-/left-handed (CRLH) mushroom structure [7]–[9]. The TM_{10} mode and antiphase TM_{20} mode are simultaneously excited with similar boresight radiation patterns. The distinguished operating principle enables the utilization of a substrate with small thickness and relatively high permittivity for broadband antenna design. Note that in such a design, the dual operating modes are both located on the right-handed (RH) dispersion branch of the CRLH mushroom structure. The left-handed (LH) branch is not necessary for such dual-mode antenna [10].

In this communication, we present a broadband low-profile metamaterial-based grid-slotted microstrip patch antenna. The aperture coupled feeding structure on the ground plane is positioned right underneath and parallel to the grid slot at the center of the patch. The radiating grid-slotted patch can be considered as a periodic structure comprising series capacitor-loaded metamaterial patch cells, which produce a pure RH dispersion branch with a zero phase constant at a finite and nonzero frequency. The TM_{10} mode and antiphase TM_{20} mode are excited in the grid-slotted patch antenna as well. Based on the dispersion relation of the capacitor-loaded patch unit cell, the effects of the variation of the slot grid and the overall patch on the antenna performance are investigated. The proposed antenna is numerically studied using CST Microwave Studio [11] and experimentally validated.

Manuscript received November 24, 2014; revised March 21, 2015; accepted April 29, 2015. Date of publication May 05, 2015; date of current version July 02, 2015. This work was supported by MOE AcRF Tier 1 Project of "Study of metadielectric and its applications" (Startup Grant).

W. Liu is with the Department of Electrical and Computer Engineering, National University of Singapore, 117583 Singapore (e-mail: eleliwe@nus.edu.sg).

Z. N. Chen is with the Department of Electrical and Computer Engineering, National University of Singapore, 117583 Singapore, and also with the Institute for Infocomm Research ($\mathrm{I}^2\mathrm{R}$), Agency for Science, Technology, and Research (A*STAR), 138632 Singapore (e-mail: eleczn@nus.edu.sg; chenzn@i2r.a-star.edu.sg).

X. Qing is with the Institute for Infocomm Research ($\mathrm{I}^2\mathrm{R}$), Agency for Science, Technology, and Research (A*STAR), 138632 Singapore (e-mail: qingxm@i2r.a-star.edu.sg).

Color versions of one or more of the figures in this communication are available online at http://ieeexplore.ieee.org.

Digital Object Identifier 10.1109/TAP.2015.2429741

II. Grid-Slotted Patch Antenna

The proposed metamaterial-based grid-slotted patch antenna is shown in Fig. 1. It is a three-layer structure where the upper and lower dielectric substrates are Rogers RO4003C with the relative permittivity of 3.38, loss tangent of 0.0027, and respective thickness of h and h_0. The rectangular microstrip patch ($L_p \times W_p$) printed onto the top layer of the upper substrate ($G_L \times G_W$) is cut up by a uniform slot grid. The number and width of the grid slots in the resonant and nonresonant directions are ($n_x,\ g_x$) and ($n_y,\ g_y$), respectively. The grid-slotted patch can be considered as a two-dimensional periodic structure of capacitor-loaded patch unit cells with a number, period, and patch width of ($m_x,\ p_x,\ w_x$) and ($m_y,\ p_y,\ w_y$) along x- and y-axes direction, separately, and $m_x = n_x + 1,\ m_y = n_y + 1,\ p_x = w_x + g_x,\ p_y = w_y + g_y, L_p = m_x p_x - g_x, W_p = m_y p_y - g_y$. The antenna is center-fed by a $50-\Omega$ microstrip line through an aperture cut in the ground plane. The slot number n_x should be odd to align the coupling aperture to the center grid slot.

The optimized dimensions of a grid-slotted patch antenna are tabulated in Table I. The whole patch is cut into a 4×4 patch array with three radiating slots and three nonradiating slots. The corresponding antenna performance is to be analyzed by considering the dispersion property of the capacitor-loaded patch unit cell. The connecting via of the unit cell is removed when compared with the metamaterial mushroom antenna [7], leading to the absence of the LH branch and preservation of the RH dispersion characterized with a zero phase constant at a specific non-zero frequency. The aperture coupled grid-slotted patch sustains TM_{10} and antiphase TM_{20} modes closely spaced at the RH dispersion branch as well. The transmission-line model is still applicable to the mode analysis of the vialess grid-slotted patch antenna, and the equations for estimating the dual-mode frequencies [7], [12] are reproduced as follows:

$$\beta_u p_x/\pi = \frac{1-2\beta_e \Delta L/\pi}{m_x}, \mathrm{TM}_{10}\ \mathrm{mode} \tag{1}$$

$$\beta_u p_x/\pi = \frac{1-2\beta_e \Delta L/\pi}{m_x/2}, \mathrm{antiphase\ TM}_{20}\ \mathrm{mode} \tag{2}$$

$$\beta_e = 2\pi f\sqrt{\varepsilon_{re}}/c \tag{3}$$

$$\frac{\Delta L}{h} = 0.412\frac{(\varepsilon_{re}+0.3)\,(W_p/h+0.262)}{(\varepsilon_{re}-0.258)\,(W_p/h+0.813)} \tag{4}$$

$$\varepsilon_{re} = \frac{\varepsilon_r+1}{2} + \frac{\varepsilon_r-1}{2}(1+12h/W_p)^{-1/2} \tag{5}$$

where f is the operating frequency, c is the speed of light in vacuum, β_u is the propagation constant of the capacitor-loaded patch unit cell, and β_e is the propagation constant in the effective extended region with a length of ΔL at each end along the resonant direction due to the effect of the fringing field.

Fig. 2 shows the dispersion diagram of the capacitor-loaded patch unit cell obtained from full-wave simulation. The simulation model

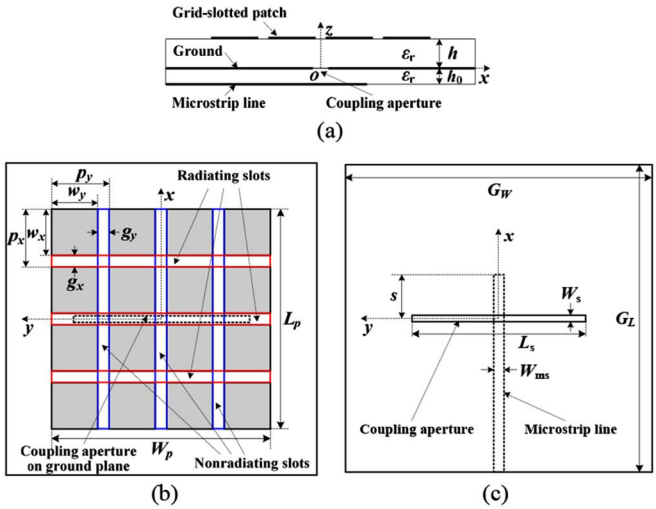

Fig. 1. Geometry of the proposed aperture-coupled grid-slotted patch antenna and the coordinate system. (a) Side view. (b) Top view of the grid-slotted patch. (c) Top view of the microstrip-line aperture coupling structure.

TABLE I
DIMENSIONS OF THE GRID-SLOTTED PATCH ANTENNA (UNIT: MM)

p_x	g_x	p_y	g_y	n_x	n_y	L_p	W_p
10	1	10	1	3	3	39	39
h	h_0	L_s	W_s	s	W_{ms}	G_L	G_W
3.25	0.813	26	2	9	1.85	60	60

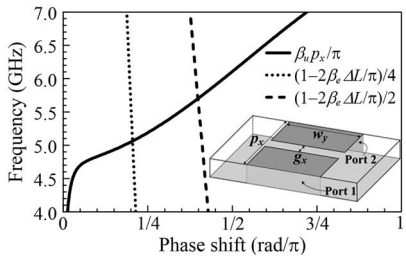

Fig. 2. Dispersion diagram of the series-capacitor-loaded patch unit cell.

of the unit cell is shown in the inset of Fig. 2. The right-hand side terms of (1) and (2) are also plotted in Fig. 2 for determining the resonant frequencies of the operating TM_{10} and antiphase TM_{20} modes. The predicted resonant frequencies of the dual modes based on the transmission-line model are 5.06 and 5.70 GHz, respectively. Fig. 3 presents the simulated $|S_{11}|$ and boresight directivity of the antenna. Two resonances appear at the frequencies of 5.07 and 5.76 GHz, which are close to the prediction. Fig. 4(a) shows the simulated E-field distributions on the plane of $y = 5$ mm at 5.07 and 5.76 GHz, in correspondence to the TM_{10} and antiphase TM_{20} modes, respectively. In the antiphase TM_{20} mode, the directions of the E-field at the opposite sides of the central aperture-slot region are antiparallel. In-phase radiation field distributions along the radiating slots and the open edges are excited for both TM_{10} and antiphase TM_{20} modes as illustrated in Fig. 4(b). The closely spaced dual modes result in broadband performance.

As shown in Fig. 3, the proposed grid-slotted patch antenna achieves a -10-dB impedance bandwidth of 29% ranging from 4.60 to 6.17 GHz. Over the bandwidth, the boresight directivity varies from 8.0 to 10.7 dBi. The performance of the reference mushroom antenna is compared in Fig. 3 as well. The reference mushroom antenna has a center-connected shorting via with a diameter of 0.6 mm for each

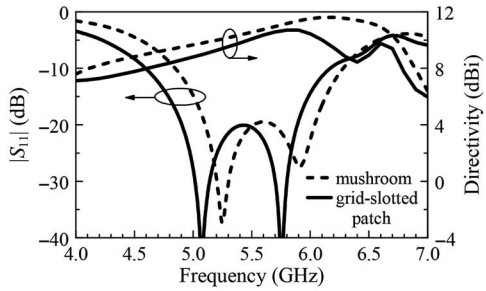

Fig. 3. Simulated $|S_{11}|$ and boresight directivity of grid-slotted patch antenna.

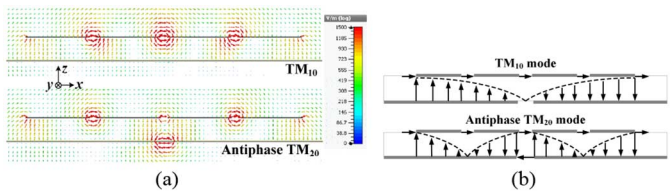

Fig. 4. TM_{10} and antiphase TM_{20} modes of the equally grid-slotted patch antenna. (a) Simulated electric field distribution on $y = 5$ mm plane at 5.07 and 5.76 GHz. (b) Sketch of the operation mechanism.

mushroom cell, and a coupling aperture of 30 mm × 1.6 mm [7]. The other dimensions are the same as the grid-slotted patch antenna. The mushroom antenna attains a boresight directivity of 9.4–11.6 dBi over the -10-dB impedance bandwidth of 4.85–6.28 GHz or 26%. The grid-slotted patch antenna can be regarded as a specific mushroom antenna with a shorting via diameter of zero. With the decrease of the shorting via diameter, the increasing effective shunt inductance in the unit cell lowers both the resonant frequencies and quality factor of the antenna. Compared with the mushroom antenna counterpart, the vialess grid-slotted patch antenna achieves a wider operating bandwidth of 29% and a lower center frequency of 5.385 GHz with the same levels of in-band return loss.

III. PARAMETRIC STUDIES

Since the dominant surface wave launched in the grounded substrate is along the E-plane of the grid-slotted patch antenna over the operating band [9], the antenna performances are affected by the ground substrate length G_L, whereas they are hardly influenced by G_W. The optimized ground substrate of 60 mm × 60 mm is fixed for the proposed antenna by taking into account the reflection coefficient, gain, and backlobe levels. In this section, the effects of the variation in the slot grid on the performance of the proposed grid-slotted patch antenna are first examined with a fixed overall patch of 39 mm × 39 mm. Then, the effect of the size of the overall microstrip patch on the antenna performance is studied. Finally, the analysis of the unequally grid-slotted patch antenna is carried out. As the dispersion property of the constituent capacitor-loaded patch cell plays a key role in the antenna performance, the changes in the dispersion diagram of the unit cell by varying the parameters p_x, w_y, and g_x are extracted as shown in Fig. 5. The proposed antenna with the dimensions listed in Table I is used as reference, and only the parameters with different values are to be addressed in the plots of the following parametric study.

A. Grid Slot Width (g_x, g_y)

The influence of different nonradiating slot widths g_y on the $|S_{11}|$ and directivity is shown in Fig. 6(a). The other dimensions are kept the same as the reference antenna. The increase in g_y corresponds to

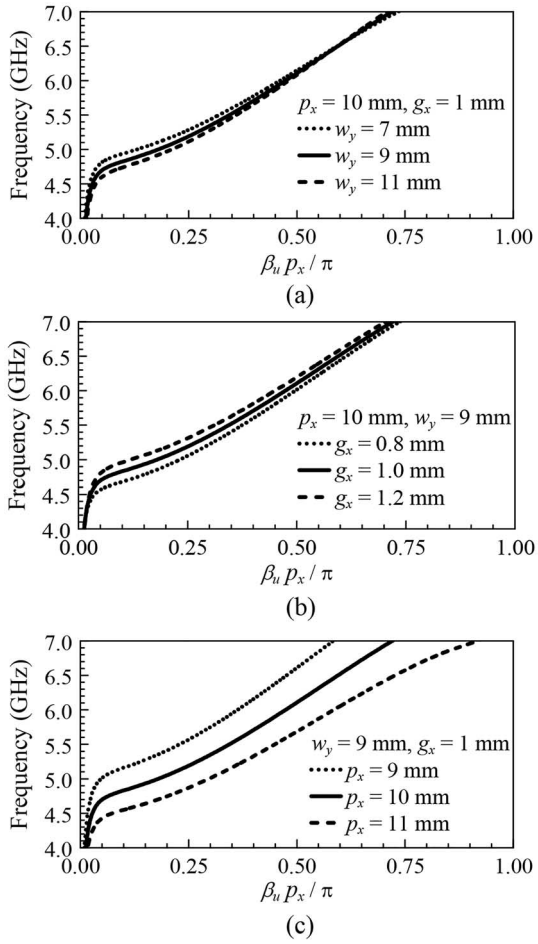

Fig. 5. Dispersion diagram of capacitor-loaded patch unit with different (a) w_y; (b) g_x; and (c) p_x.

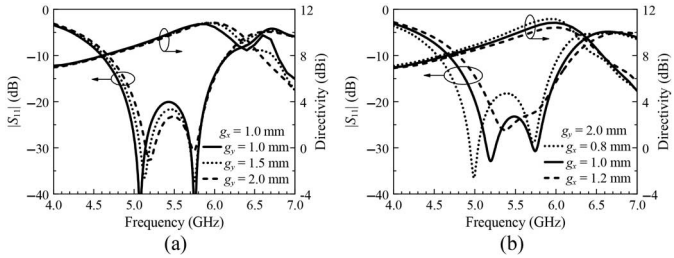

Fig. 6. $|S_{11}|$ and boresight directivity with different (a) g_y and (b) g_x.

the decrease of patch width w_y. With the decrease in w_y, the lower part of the RH dispersion branch is shifted to higher frequencies while the higher part around $\beta_u p_x = \pi/2$ is almost unchanged as shown in Fig. 5(a). The change tendency of the dispersion relation indicates that the TM_{10} mode resonant frequency increases with the increment of g_y while the antiphase TM_{20} mode resonant frequency is hardly affected, as shown in Fig. 6(a). It is also seen from the directivity curves that the directivity degradation at the higher frequencies, resulting from the higher order mode along the nonresonant direction, is improved when g_y increases from 1.0 to 2.0 mm.

The effect of the radiating slot width g_x on the dispersion relation is examined with $g_y = 2.0$ mm. From the RH dispersion branch as shown in Fig. 5(b), the frequencies become lower when g_x changes from 1.2 to 0.8 mm. Therefore, the operating band of the antenna shifts to lower frequencies with the decrement of radiating slot width

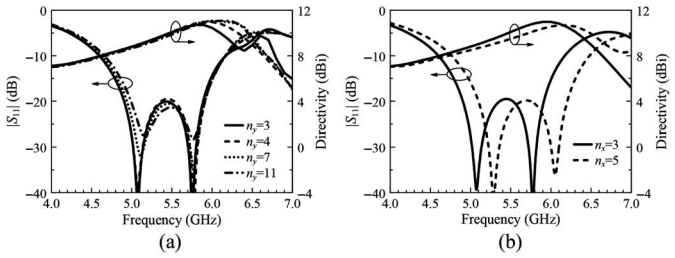

Fig. 7. $|S_{11}|$ and boresight directivity with different (a) nonradiating slot number n_y and (b) radiating slot number n_x ($n_x = 3$, $n_y = 4$, $g_x = 1$ mm, $L_s = 26$ mm, $s = 9$ mm; $n_x = 5$, $n_y = 4$, $g_x = 0.3$ mm, $L_s = 24$ mm, $s = 8.5$ mm).

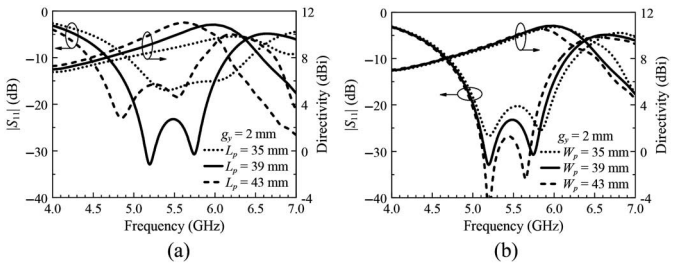

Fig. 8. $|S_{11}|$ and boresight directivity with different (a) L_p and (b) W_p.

as reflected in Fig. 6(b). The directivity increases with a more uniform field distribution on the antenna surface because of the smaller radiating slot width.

B. Grid Slot Number (n_x, n_y)

Fig. 7(a) shows the $|S_{11}|$ and directivity of the antenna with increasing nonradiating slot number n_y. As the overall patch is equally cut up by the slot grid, the increase in n_y corresponds to the decrease in w_y. Therefore, similar results are found both with increasing the width g_y and number n_y of the nonradiating slots. The higher order mode along the nonresonant direction is eliminated from the operating bandwidth as well by cutting more nonradiating slots.

Consider five radiating slots etched on the overall patch to check the effect of the radiating slot number n_x on the antenna performance. Four nonradiating slots are used in both antennas with $n_x = 3$ and $n_x = 5$. For the antenna with five radiating slots, smaller radiating slot width g_x of 0.3 mm is used to sustain a uniform field distribution on the top surface with the optimized feed dimensions of $L_s = 24$ mm and $s = 8.5$ mm. The $|S_{11}|$ and directivity of the proposed antenna with $n_x = 5$ and $n_x = 3$ are compared in Fig. 7(b). Almost the same fractional bandwidth for both return loss and directivity is achieved with more radiating slots of smaller width.

C. Size of Overall Patch (L_p, W_p)

The size of the overall patch on the antenna performance is studied, where the patch is equally cut up by a slot-grid with $g_y = 2$ mm. When the length of the constituent unit cell p_x increases, the whole RH dispersion branch shifts down to lower frequencies as shown in Fig. 5(c). Therefore, the increment in the overall patch length L_p results in a considerable downshift in the operating bandwidth of the antenna as plotted in Fig. 8(a). The directivity increases with a longer patch because of the enlarged effective radiating aperture.

Fig. 8(b) shows the $|S_{11}|$ and directivity with varying overall patch width W_p. When the overall patch width W_p increases from 35 to

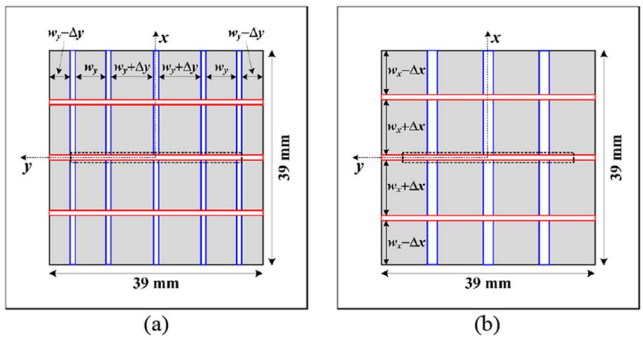

Fig. 9. Unequally grid-slotted patch antenna. (a) Nonuniform-distributed non-radiating slots. (b) Non-niform-distributed radiating slots.

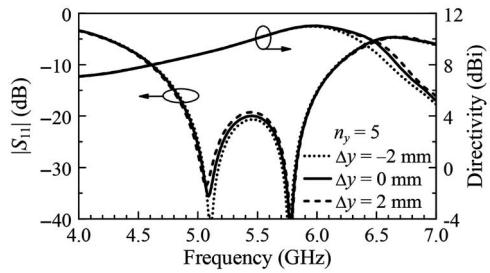

Fig. 10. $|S_{11}|$ and boresight directivity of the antenna unequally slotted along nonresonant direction.

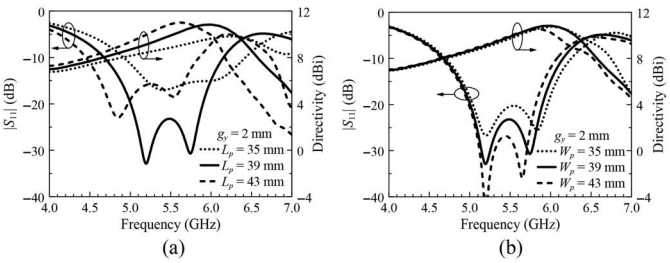

Fig. 11. Antenna unequally slotted along resonant direction. (a) $|S_{11}|$ and boresight directivity. and (b) Input impedance.

43 mm, the upper resonant frequency decreases from 5.84 to 5.65 GHz, while the lower resonant frequency is hardly affected.

D. Unequally Grid-Slotted Patch (Δx, Δy)

The overall patch of all the aforementioned antennas is equally cut up by a slot grid. Herein, we investigate the performance of the unequally grid-slotted patch antenna. As shown in Fig. 9(a), the antenna with five nonradiating slots symmetrically but unequally spaced along nonresonant direction is taken into account. As suggested in Fig. 10, the nonuniform distribution of the nonradiating slots has a slight effect on the impedance matching and directivity of the antenna.

Consider the grid-slotted patch antenna unequally cut up by three radiating slots. Three nonradiating slots with $g_y = 2$ mm are equally spaced along the nonresonant direction. The center-radiating slot is still cut at the center of the overall patch. The two side-radiating slots are shifted from the quarter-length positions as shown in Fig. 9(b). The impedance matching of the antenna is sensitive to shifting the side-radiating slots as plotted in Fig. 11. As the side-radiating slots

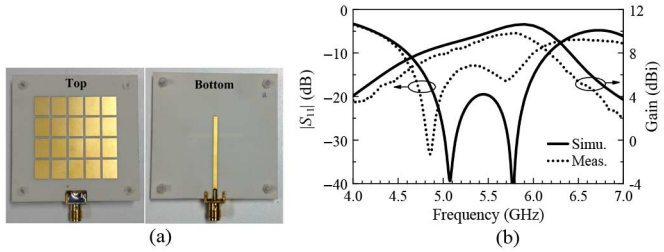

Fig. 12. (a) Photograph of antenna prototype. (b) $|S_{11}|$ and gain.

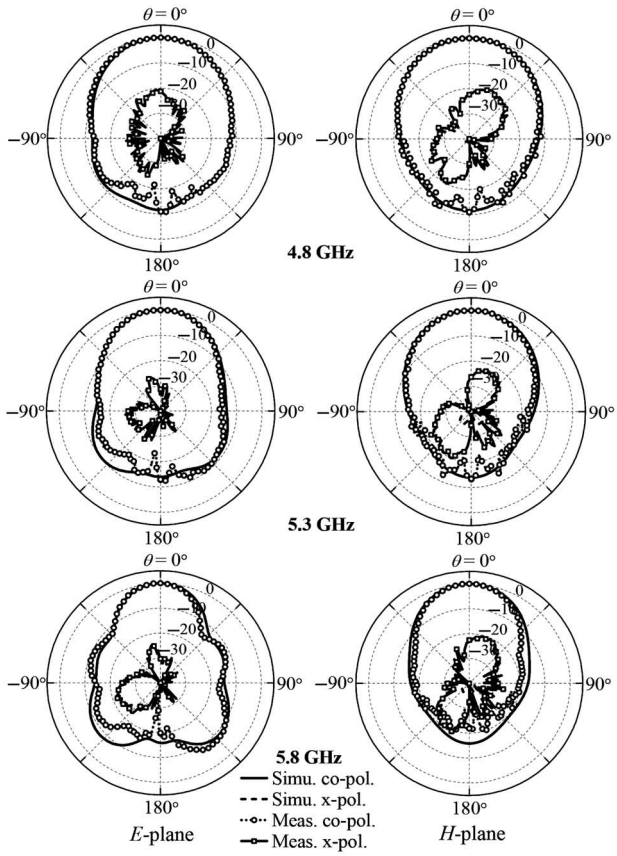

Fig. 13. Radiation patterns at 4.8, 5.3, and 5.8 GHz.

moving to the edges, the input resistance increases and the input reactance exhibits larger ripple over the operating bandwidth, leading to a widened -10-dB impedance bandwidth but increased in-band return loss. The directivity at the higher part of the bandwidth is deteriorated when the side radiating slots are shifted away from the quarter-length positions.

IV. Experimental Results

In order to validate the proposed antenna design, a microstrip-line aperture coupled equally grid-slotted patch antenna was prototyped and measured. The antenna prototype has the same dimensions as those listed in Table I, except the use of four nonradiating slots. Fig. 12(a) shows the prototype of the antenna with an overall size of $60 \text{ mm} \times 60 \text{ mm} \times 4.1 \text{ mm}$.

Fig. 12(b) illustrates the simulated and measured reflection coefficient and realized gain of the antenna. Over the simulated -10-dB impedance bandwidth of 4.60–6.17 GHz or 29%, the simulated gain

ranges from 7.4 to 10.6 dBi. The simulated radiation efficiency is higher than 92% over the bandwidth ranging from 4.60 to 6.17 GHz with a peak efficiency of 97% around 5 GHz. The measured -10-dB impedance bandwidth is from 4.54 to 6.00 GHz or 28% with the measured gain ranging from 6.0 to 9.8 dBi. Reasonable agreement is observed between the simulated and the measured results. The slight downward shift of the operating frequencies may come from the increased actual dielectric constant of the substrate, the fabrication and/or assemble tolerance of the antenna.

The simulated and measured radiation patterns of the antenna at 4.8, 5.3, and 5.8 GHz are exhibited in Fig. 13. The measured copolarization patterns are in good coincidence with the simulation. The simulated cross-polarization levels are less than -130 dB in the E-plane and -33 dB in the H-plane. The measured cross-polarization levels are below -20 dB in both the E- and H-planes. The discrepancy between the simulated and the measured cross-polarization levels may be caused by the SMA connector and the measurement environment. In general, consistent boresight radiation with low cross-polarization level is achieved over the entire operating bandwidth.

V. Conclusion

A broadband low-profile aperture coupled metamaterial grid-slotted patch antenna has been proposed. Transmission-line model integrated with the dispersion relation of the constituent capacitor-loaded patch cells has been applied in the analysis of the dual-operating modes. The effects of the variations in the overall patch and slot-grid on the antenna performance have been investigated. The backlobe levels can be further suppressed using an aperture coupling structure with a shielding plane such as stripline and substrate integrated waveguide if required. This vialess compact broadband radiator can be employed in satellite, radar, and wireless communication systems.

References

[1] P. S. Hall, "Probe compensation in thick microstrip patches," *Electron. Lett.*, vol. 23, no. 11, pp. 606–607, May 1987.

[2] K. M. Luk, C. L. Mak, Y. L. Chow, and K. F. Lee, "Broadband microstrip patch antenna," *Electron. Lett.*, vol. 34, no. 15, pp. 1442–1443, Jul. 1998.

[3] S. D. Targonski and D. M. Pozar, "Design of wideband circularly polarized aperture-coupled microstrip antennas," *IEEE Trans. Antennas Propag.*, vol. 41, no. 2, pp. 214–220, Feb. 1993.

[4] K. F. Lee *et al.*, "Experimental and simulation studies of the coaxially fed U-slot rectangular patch antenna," *IEE Proc. Microwaves Antennas Propag.*, vol. 144, no. 5, pp. 354–358, Oct. 1997.

[5] F. Croq and A. Papiernik, "Stacked slot-coupled printed antenna," *IEEE Microw. Guided Wave Lett.*, vol. 1, no. 10, pp. 288–290, Oct. 1991.

[6] D. Sun, W. Dou, L. You, X. Yan, and R. Shen, "A broadband proximity-coupled stacked microstrip antenna with cavity-backed configuration," *IEEE Antennas Wireless Propag. Lett.*, vol. 10, pp. 1055–1058, Oct. 2011.

[7] W. Liu, Z. N. Chen, and X. Qing, "Metamaterial-based low-profile broadband mushroom antenna," *IEEE Trans. Antennas Propag.*, vol. 62, no. 3, pp. 1165–1172, Mar. 2014.

[8] W. Liu, Z. N. Chen, and X. Qing, "Stripline aperture coupled metamaterial mushroom antenna with increased front-to-back ratio," in *Proc. IEEE Int. Symp. Antennas Propag. USNC-URSI Radio Sci. Meeting*, Memphis, TN, USA, Jul. 6–12, 2014, pp. 444–445.

[9] W. Liu, Z. N. Chen, and X. Qing, "60-GHz thin broadband high-gain LTCC metamaterial-mushroom antenna array," *IEEE Trans. Antennas Propag.*, vol. 62, no. 9, pp. 4592–4601, Sep. 2014.

[10] C. Caloz and T. Itoh, *Electromagnetic Metamaterials: Transmission Line Theory and Microwave Applications*. Hoboken, NJ, USA: Wiley, 2006.

[11] *CST Microwave Studio, Computer Simulation Technology* [Online]. Available: http://www.cst.com/Content/Products/MWS/Overview.aspx

[12] E. O. Hammerstad, "Equations for microstrip circuit design," in *Proc. 5th Eur. Microwave Conf.*, Hamburg, West Germany, Sep. 1–4, 1975, pp. 268–272.